Size-dependent selectivity of Cu2O nanocube catalysts for CO2 reduction at industrial current densities

Electrochimica Acta 551 (2026) 148114

Contents lists available at ScienceDirect

Electrochimica Acta

journal homepage: www.journals.elsevier.com/electrochimica-acta

Size-dependent selectivity of Cu_2O nanocube catalysts for CO_2 reduction at industrial current densities

Marco Etzi [a,b,*], Alessio Mezza [a,c], Valentina Bugliarelli [a,c], Julien Dangbegnon [a], Daniele Sassone [a], Mattia Bartoli [a,b], Juqin Zeng [a,c], Angelica Chiodoni [a], Sergio Bocchini [a,b,c], Adriano Sacco [a], Candido Fabrizio Pirri [a,c]

[a] Center for Sustainable Future Technologies (CSFT@Polito), Istituto Italiano di Tecnologia, Via Livorno 60, 10144 Torino, Italy
[b] Consorzio Interuniversitario Nazionale per la Scienza e Tecnologia dei Materiali (INSTM), Via G. Giusti 9, 50121 Florence, Italy
[c] Department of Applied Science and Technology, Politecnico di Torino, Corso Duca degli Abruzzi 24, 10129 Torino, Italy

ARTICLE INFO

Keywords:
Copper
CO_2 reduction
Electrochemistry
Ethylene
Nanocube catalyst

ABSTRACT

The electrochemical reduction of CO_2 (CO_2RR) to value-added chemicals offers a promising route for carbon recycling and renewable energy storage. Cu-based catalysts are uniquely capable of producing multi-carbon products such as ethylene, but their selectivity is highly sensitive to their morphology. In this work, we systematically investigate the impact of Cu_2O nanocube size (45–600 nm) on CO_2RR performance in both alkaline flow cell and zero-gap electrolyzer, both operating at industrially-relevant current densities. The catalysts were synthesized with well-controlled geometries and edge lengths. In the flow-cell, smaller nanocubes (45–75 nm) exhibited superior selectivity toward ethylene and liquid C_2 products, achieving Faradaic efficiencies toward C_2 products (FE_{C2}) of up to 50%, attributed to an optimal balance between edge and facet sites. In contrast, in the zero-gap cell, although 45 nm cubes were the most ethylene-selective, overall FE_{C2} was reduced and strongly influenced by operational parameters, such as anolyte composition. Long-term tests revealed a trade-off between catalyst durability and ethylene selectivity. These findings demonstrate the critical interplay between nanostructure, testing configuration, and electrolyte, and emphasize the need to assess catalyst performance under industrially-relevant conditions.

1. Introduction

The electrochemical reduction of CO_2 (CO_2RR) has emerged as a pivotal technology for sustainable carbon management and renewable energy conversion [1]. Electrocatalysts play an important role in determining the selectivity of the reaction toward specific reduction products [2]. Among the various electrocatalysts explored for this purpose, copper (Cu) stands out due to its ability to selectively produce valuable hydrocarbons and oxygenates, particularly C_{2+} products, under electrochemical conditions [3]. These unique properties of Cu are due to its intermediate CO binding energy, following Sabatier's principle [4,5]. The intrinsic properties of Cu are highly sensitive to its surface morphology, which significantly influences product selectivity during CO_2RR [6–9].

Notably, the presence of specific crystal facets (facet-effect), such as the (111), (100), and (110) surfaces, has been linked to distinct pathways for C—C bond formation and subsequent product distribution, favoring methane, ethylene, and oxygenated hydrocarbons, respectively [10–13].

However, it is important to control not only the surface structure of Cu but also the size of the nanostructures employed. Previous research on the size-dependency of CO_2RR selectivity of Cu catalysts led to conflicting results. Manthiram et al. reported improved methanation activity of 7 nm Cu nanoparticles (NPs) as compared to Cu foil [14]. On the other hand, Reske et al. found that hydrocarbon (both methane and ethylene) production was increasingly suppressed for smaller spherical NPs (up to 5 nm) [15]. These results emphasize that the change in the laboratory testing setups could lead to substantially different experimental outcomes and conclusions.

Cu_2O nanocubes, with their well-defined geometry, present an ideal platform for investigating how these factors influence the selectivity of CO_2RR [13]. In particular, the size of the nanocubes can alter surface

* Corresponding author at: Center for Sustainable Future Technologies (CSFT@Polito), Istituto Italiano di Tecnologia, Via Livorno 60, 10144 Torino, Italy.
E-mail address: marco.etzi@iit.it (M. Etzi).

https://doi.org/10.1016/j.electacta.2026.148114
Received 22 October 2025; Received in revised form 15 December 2025; Accepted 1 January 2026
Available online 2 January 2026

atom arrangements and the availability of active sites, potentially enhancing the kinetics of relevant reaction intermediates. Furthermore, the local electrochemical environment, influenced by factors such as pH and ionic strength, also plays a critical role in modulating the performance and selectivity of the nanostructured catalysts.

In a previous work, Loiudice et al. found that Cu nanocubes with an edge length of 44 nm exhibit the highest Faradaic Efficiency (FE) toward ethylene among 24, 44, and 63 nm cubes [16]. The reason for the boosted C_2 production was attributed to the optimal ratio between edge and plane sites. Furthermore, the initial edge length of Cu nanocubes influences their long-term stability; larger nanocubes (580 nm) experience significant reconstruction and a more rapid decline in the CO_2RR to hydrogen evolution ratio compared to 280 nm cubes [17]. For Cu_2O cubes with sizes ranging from 80 to 390 nm, fragmentation, detachment, aggregation, and redeposition processes occur, though to different extents depending on the initial edge length of the cubes; specifically, 170 nm Cu_2O cubes were found optimal for the production of C_{2+} products due to the limited detachment and aggregation combined with a high density of re-deposited particles [18]. These aspects are particularly important for the future scaling up of CO_2 electrolyzers, where catalysts should operate at high current densities for prolonged periods.

In much of the existing literature, the size effect of nanocubes has been assessed using standard H-cells, where the resulting current densities (j) typically range from a few mA cm^{-2} to tens of mA cm^{-2} [17–20]. However, evaluating catalysts in flow cells or zero-gap electrolyzers provides insights into their catalytic activity, stability, and selectivity at industrially relevant current densities (i.e., $j \geq 200$ mA cm^{-2}) [21]. These setups address the limited solubility of CO_2 in aqueous electrolytes by directly supplying CO_2 gas to the back of a gas diffusion electrode (GDE) [22–25]. Product distribution is highly sensitive to the setup, as high current densities induce fast catalyst restructuring [26, 27]. Moreover, van der Veer et al. showed that GDE flooding, a typical reason for electrode failure, is fastened by the roughening induced by high current densities used in flow cells [27].

In this study, we systematically investigate the influence of Cu_2O nanocube size on the product selectivity of the CO_2 reduction reaction. By synthesizing a series of nanocubes with varying edge lengths, we aim to elucidate the structure-activity relationships that direct their performance in two different setups, namely in flow and zero-gap electrolyzers. Although the selectivity is strongly dependent on the setup, we found an optimal size range of cubes for boosted ethylene production. Our findings will contribute to the broader understanding of how nanostructure design affects the selectivity and efficiency of CO_2 reduction processes, thereby advancing the potential for practical applications in carbon recycling and renewable energy.

2. Experimental

2.1. Materials

$CuSO_4 \cdot 5H_2O$ (Merck, 99 % min.), $CuCl_2$ (Sigma Aldrich, 99 %), trisodium citrate dihydrate (Sigma Aldrich, 99 %), NaOH (Sigma Aldrich, 98 %), ascorbic acid (Sigma Aldrich, 98 %), isopropanol (Sigma Aldrich, 99.8 %), KOH (Sigma Aldrich, 84 % min.) were used without further purification. Milli-Q water (18.2 MΩ·cm) was used for solution preparation.

2.2. Synthesis

Different syntheses were performed to obtain Cu_2O nanocubes with different edge lengths.

Smaller nanocubes (in the range of 45–75 nm) were prepared following the procedure reported by Chang et al. [28], using trisodium citrate as chelating agent to tune the nanocube size. Briefly, 400 mL of deionized water was put in a beaker, and different amounts of a 1.2 M trisodium citrate solution were added: 0 mL for the 45 nm cubes and 0.75 mL for the 75 nm cubes. The solution was stirred for 20 min at room temperature. Then, 1 mL of 1.2 M $CuSO_4 \cdot 5H_2O$ solution was added, followed by stirring for 5 min to obtain a pale blue color. 1 mL of 4.8 M NaOH was then added to the solution, inducing the rapid formation of $Cu(OH)_2$ with an intense blue color. After stirring for 5 min, 1 mL of 1.2 M ascorbic acid solution was added as a reducing agent. The color of the solution gradually changed to orange within 30 min. Finally, the solid products were collected after centrifugation of the solution at 4200 rpm for 20 min. The products were subsequently washed and centrifuged three times (twice in water, once in ethanol). The product was then dried overnight in a vacuum oven set at 40 °C.

Larger nanocubes (600 nm) were obtained using the procedure described by Gao et al. [29]: briefly, 1 L of 0.01 M $CuCl_2$ solution was placed in a round-bottom flask, heated at 55 °C in an oil bath, and kept under vigorous stirring. Then, 100 mL of 2 M NaOH was added dropwise. After stirring for 30 min, 100 mL of a 0.6 M ascorbic acid solution was added dropwise, leading to a gradual change from brownish to reddish color. The solution was maintained at 55 °C under stirring for 3 h. After cooling, the product was separated by using the centrifugation method employed for the small nanocubes and described above.

Intermediate nanocubes (450 nm) were obtained using a modified procedure by Gao et al. [29] (employed for the 600 nm nanocubes), utilizing a lower amount of copper salt, 5 mM $CuCl_2$ solution, and keeping all the other parameters equal. The list of synthesized catalysts is reported in Table 1.

2.3. Electrochemical tests in flow cell

Gas diffusion electrodes (GDEs) for tests in a flow cell configuration were prepared on Freudenberg H23C6 gas diffusion layer (GDLs) purchased from Fuelcellstore. An ink with 2.5 mg of catalyst, 12.5 μL of Nafion 5 wt % solution (Sigma Aldrich), and 400 μL of isopropanol was prepared and sonicated until a homogenous suspension was obtained. Then, a volume of 40 μL of ink was deposited by drop-casting on a 0.5 cm^2 delimited area of GDL while keeping the substrate on a hot plate ($T \approx 80$ °C). The catalyst loading was 0.5 mg cm^{-2}.

Electrochemical tests were performed in a flow cell manufactured by Electrocell at room temperature (Fig. S1). The Cu-based GDE, an IrO_2-coated titanium plate, and an Ag/AgCl (3 M Cl^-) electrode were used as working, counter, and reference electrodes, respectively. A Fumasep FAB-PK-130 anionic exchange membrane (AEM) was used to separate the cathodic and anodic compartments. Electrochemical tests were performed using a Biologic SP-300 potentiostat. The experiment time was 45 min unless otherwise indicated. The 45-minute electrolysis period was selected to efficiently screen the different catalyst sizes and current densities and to allow reliable quantification of all gaseous and liquid products under steady-state conditions, considering that CO_2 electrolysis at high current density, in its current state of development, is prone to specific failure modes irrespective of the setup and catalyst employed [30]. Current densities were normalized to the geometric area of the electrodes.

A KOH (Sigma-Aldrich, 84 % min.) 1 mol L^{-1} solution was used as both catholyte and anolyte and pumped through the electrode compartments at a flow rate of 1 mL min^{-1} using a peristaltic pump. CO_2 was fed at the back of the cathode at a flow rate of 15 mL min^{-1} using a Bronkhorst mass flow controller.

Gas-phase products were analyzed by an online micro gas

Table 1
List of synthesized catalysts.

Nominal cube edge length / nm	Ref.
45	[28]
75	[28]
450	modified from [29]
600	[29]

chromatograph (μGC, Fusion®, INFICON) with two channels containing a 10 m Rt-Molsieve 5 A column and an 8 m Rt-Q-Bond column. Both channels were equipped with a micro-thermal conductivity detector (micro-TCD).

The Faradaic efficiency (FE) for each gas product was calculated using the following equation:

$$FE\ (\%) = \frac{z\ F\ X\ f}{I} \times\ 100$$

where z is the number of transferred electrons to form each specific product (2 for H_2 and CO, 8 for CH_4, 12 for C_2H_4), F is the Faraday constant (96,485 C mol^{-1}), X is the mole fraction of the gas product in the flow, f is the total gas flow (mol s^{-1}) measured at the μGC inlet, and I is the total applied current.

The liquid products were collected and analyzed by high-performance liquid chromatography (Shimadzu Prominence HPLC) equipped with a Repromer H column with pre-column, using 9 mM H_2SO_4 as mobile phase. The Faradaic efficiency of each liquid product was calculated using the following equation:

$$FE\ (\%) = \frac{z\ F\ C\ V\ d}{10^6\ MM\ Q} \times\ 100$$

where z is the number of transferred electrons to form each specific product (2 for $HCOO^-$, 12 for C_2H_5OH), C is the measured concentration (in ppm) of the product in the total volume of electrolyte, V is the total volume of electrolyte (in mL) collected at the end of each test, d is the density (in g mL^{-1}) of the product, MM is the molar mass (in g mol^{-1}) of the product, and Q is the total charge (in C).

Error bars were obtained by averaging the FEs of at least two to three independent samples for each GDE.

2.4. Electrochemical tests in zero-gap cell

Gas diffusion electrodes (GDEs) for tests in a zero-gap configuration were prepared on Sigracet 28BC gas diffusion layer (GDLs) purchased from Fuelcellstore. An ink containing catalyst, Sustainion 5 wt % solution as binder (Dioxide Materials), and solvent (75 vol % of isopropanol and 25 vol % of water) was prepared and sonicated until a homogenous suspension was obtained. The binder accounts for 2.7 wt % out of the total catalyst and binder loading.

The ink was spray-coated on a 5 cm^2 area of GDL using a spray coater (Nadetech) until the targeted catalyst loading was reached. Catalyst loading was set at 0.5 mg cm^2 and was checked by weighing the GDEs before and after spray deposition. GDEs were tested in a zero-gap cell (Dioxide Materials), where the Membrane Electrode Assembly (MEA) was prepared by sandwiching an AEM (Sustainion X37, Dioxide Materials) between the Cu-based GDE and an IrO_2-coated Ti mesh (catalyst loading: 3 mg cm^{-2}). Both electrodes were secured in PTFE gaskets, and the cell was tightened to a torque of 4 Nm. The performance of the cell was investigated through chronopotentiometry at 250 mA cm^{-2} using a Biologic HCP-103 potentiostat. The current density was normalized to the geometric area of the electrode. Gaseous humidified CO_2 was delivered to the cathode at 100 mL min^{-1} via a mass flow controller (Bronkhorst EL-FLOW), and the outlet stream was monitored by a mass flow meter (Bronkhorst EL-FLOW) and directed to an online micro gas chromatograph (μGC, Fusion®, INFICON) for product quantification. A 0.1 M $KHCO_3$ solution was used as the anolyte and recirculated on the anodic side of the cell using a peristaltic pump at a flow rate of 40 mL min^{-1}. The test was carried out until the maximum concentration of C_2H_4 was detected in the outlet stream. The anolyte was sampled at the end of the test to quantify liquid products using high-performance liquid chromatography (Shimadzu Prominence HPLC), as described above. Long-term tests were performed under the same conditions, replacing 0.1 M $KHCO_3$ with 0.1 M $CsHCO_3$ as the anolyte, and continued until a significant decrease in CO_2RR efficiency was observed.

2.5. Materials characterization

Field Emission Scanning Electron Microscopy (FESEM) images were acquired using a Zeiss Supra at an accelerating voltage of 5 kV. The edge length of nanocubes was measured using ImageJ software.

X-ray Diffraction (XRD) patterns were acquired in a Bragg-Brentano geometry using a Panalytical Xpert Pro instrument (Cu-Kα radiation, voltage 40 kV, current 40 mA) equipped with an X' Celerator 1D detector in a 2θ range of 20–80° with a step size of 0.026°

X-Ray Photoelectron Spectroscopy (XPS) spectra were acquired using a PHI 5000 Versaprobe instrument equipped with a monochromatic Al-Kα (1486.6 eV) X-ray source. An electron gun and an Ar ion gun were used for charge compensation. The spot size was 100 μm. The pass energy for the acquisition of high-resolution spectra was set at 23.5 eV. Calibration of the binding energy axis was performed by setting the position of the adventitious C 1s sp^3 peak at 284.8 eV. The spectra were processed using CasaXPS Software (v2.3.23, Casa Software Ltd).

Raman measurements were carried out using a LabRAM Soleil equipped with a 785 nm laser line with a 100 × objective in the range from 100 to 900 cm^{-1}.

3. Results and discussion

3.1. Materials characterization

Cu_2O nanocubes with edge sizes ranging from 45 to 600 nm were synthesized through two different synthesis techniques. For the small cubes (45–75 nm), the size can be controlled by varying the amount of trisodium citrate, which acts as a chelating agent and decreases the amount of Cu_2O seeds but leads to bigger nanocubes [28]. For the larger cubes (450–600 nm), the Cu salt concentration is the determining factor.

The as-prepared materials were characterized by XRD to gain insights into their crystalline structure. All fresh powders exhibit diffraction peaks at 2θ angles of 29.6°, 36.5°, 61.4°, 73.6°, 77.4°, that are ascribed to Cu_2O phase (COD #96–100–0064) (Fig. 1).

No peaks attributable to other Cu phases are visible in the diffractograms of the fresh catalysts, indicating that the synthesis procedures led to the formation of the desired products.

XPS was employed to gain insights into the surface composition of spectra of selected samples. Cu 2p spectra of fresh catalysts (Fig. S2a) show peaks of Cu $2p_{3/2}$ and Cu $2p_{1/2}$ at binding energies of ≈ 932.4 eV and ≈ 952.3 eV, respectively, which are ascribed to Cu^0 or Cu^+ species [31–34]. To distinguish between the presence of these two reduced Cu species, we acquired Cu Auger spectra (Fig. S2b). The main peaks at kinetic energies of ≈ 916.7 eV indicate that Cu is present as Cu^+ [33], in

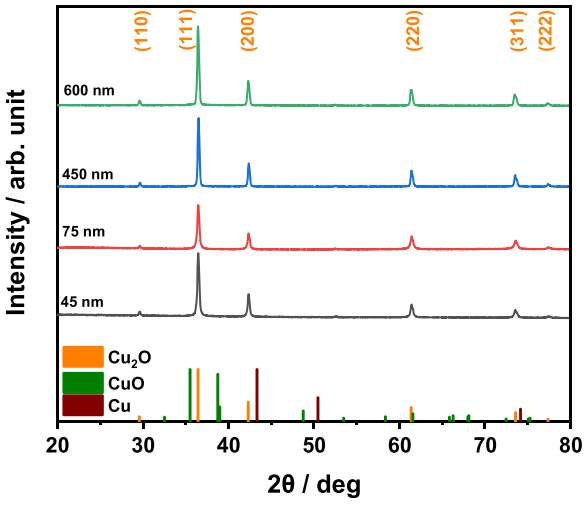

Fig. 1. XRD of as-prepared powdered catalysts.

agreement with the XRD data that pointed out the formation of Cu_2O phase. All samples consist of Cu_2O cubes, differing mainly in particle size as indicated by variations in edge length.

The morphology and size distribution of the as-prepared particles were analyzed by FESEM (Fig. 2).

All the catalysts exhibit a well-defined cubic shape, meaning that both the syntheses are well-suited to obtain Cu_2O nanocube catalysts. The size distribution of the particles is reported in Fig. S3, and shows a narrow particle size distribution, especially for the smaller cubes (45 nm and 75 nm), while the bigger cubes also have a broader size distribution. We highlight here that the latter cubes have been obtained through a longer and higher-temperature reaction, which might account for the broader size distributions obtained for the large cubes.

3.2. Electrocatalytic tests in flow cell

To investigate how different edge lengths of Cu_2O influence the catalytic activity, we performed CO_2RR experiments in alkaline conditions (KOH 1 M) using a flow cell reactor. The FEs of the main products measured at different current densities are reported in Fig. 3, while the chronopotentiometries are shown in Fig. S4.

We investigated the performance of the catalysts at three industrially relevant current densities (−150, −250, and −350 mA cm^{-2}) to capture their behavior across the range typically targeted in practical CO_2 electrolysis systems. To contextualize our results within the state of the art, Table S1 reports representative ranges of faradaic efficiencies, nanoparticle sizes, and operating conditions for Cu_2O cube–based catalysts as documented in the literature.

In Cu-based CO_2RR systems, FEs frequently sum to values below 100 %, especially at high current densities. This behavior arises from the exceptionally broad product distribution characteristic of Cu catalysts, which can generate numerous highly reduced liquid products (e.g., methanol, n-propanol, acetaldehyde, formaldehyde) at trace concentrations. Although these compounds often appear at ppm levels and may fall below standard detection limits, their formation requires a large number of electrons such that even small amounts can account for a non-negligible portion of the total charge. Additional FE losses can result from product crossover, retention in tubing or membrane interfaces, volatilization during gas–liquid separation, and other system losses.

Regardless of the current density, FE_{H2} is higher for bigger cubes than for smaller cubes. On the other hand, FE_{CO} decreases while increasing the edge length of nanocubes, in agreement with previous works [18]. For the other C_1 products, formate and methane, the selectivities are low (below 10 %). Regarding C_{2+} products, we reported the FEs for ethylene, ethanol, and acetate, since other C_{2+} products were detected only in traces. At the lowest current density explored (i.e., –150 mA cm^{-2}), the highest FE_{C2H4} was found for cubes with an edge length of 75 nm and then decreased for bigger cubes; the FE of ethanol is also the highest for 75 nm cubes, where it reaches a plateau and does not further change for the other edge lengths.

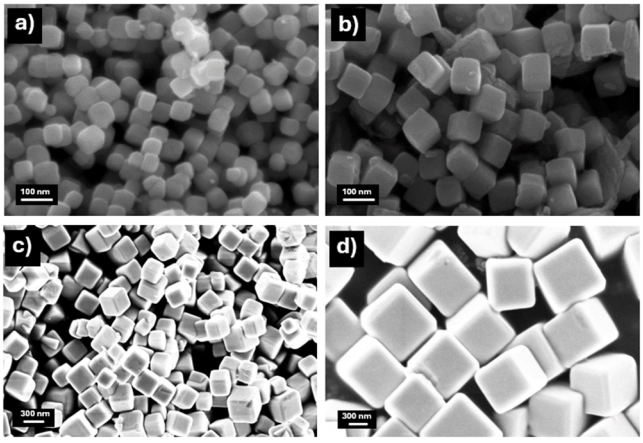

Fig. 2. FESEM images of as-prepared Cu_2O nanocubes with different edge lengths: a) 45 nm; b) 75 nm: c) 450 nm; d) 600 nm.

At higher current densities, the selectivities are more affected by the changes in the edge length of the nanocubes. At j = –250 mA cm^{-2}, the trends of H_2 and CO selectivities are similar to those recorded at –150 mA cm^{-2}, with the former increasing and the latter decreasing at larger edge lengths. For all the samples, FE_{CO} is, however, lower than that recorded at lower current density. On the other hand, the FE of C_2 products increases due to the boosted C—C coupling at more negative potentials [35]. In this case, the FE of ethylene peaks at edge lengths of 75 nm and then drastically drops for cubes of larger sizes.

At j = –350 mA cm^{-2}, H_2 production again increases and CO selectivity decreases with increasing edge lengths, though the decrease in CO production with the size is slighter than at lower current densities. Ethylene selectivity also gradually decreases and reaches a plateau at edge lengths of 450 nm.

The highest FEs for C_2 products (50 % ± 1 %) were obtained for cubes of 45 and 75 nm edge lengths at –350 mA cm^{-2} and for 75 nm cubes at –250 mA cm^{-2}. Despite the lower overpotential required by smaller cubes to reach the same current density (Fig. S4), no direct correlation between potential and product selectivity is observed. This indicates that the selectivity trends arise primarily from morphology-dependent reconstruction and the nature of the resulting active sites, rather than from differences in applied potential during chronopotentiometry. Loiudice et al. previously identified 44 nm Cu nanocubes as those with the highest FE_{C2H4} among 24, 44, and 63 nm edge lengths, due to their optimal balance between plane- and edge-sites [16]. Although from our results the 75 nm cubes seem to be slightly more selective, especially at –250 mA cm^{-2}, this discrepancy can be explained by the higher current densities (≈50–100 times higher) employed in our setup, which can induce profound catalyst reconstruction, as we will discuss below.

3.3. Materials characterization after electrocatalytic tests in flow cell

We then analyzed the catalysts after the electrocatalytic tests with XRD and FESEM to gain insights into the changes in morphology and crystalline structure induced by electrochemical polarization.

The XRD patterns of electrodes after the electrochemical tests are reported in Fig. S5. After CO_2RR, the characteristic Cu_2O peaks decrease in intensity while metallic Cu peaks emerge, confirming a partial electrochemical reduction of Cu^+ to Cu^0 under CO_2 reduction conditions [36–38]. Nevertheless, Cu_2O is still present, in agreement with a previous observation that oxide-derived Cu rapidly reoxidizes after electrolysis [39]. Residual Cu^+ species may persist even after CO_2RR experiments [9] and are essential for C_2 product formation as they can stabilize adsorbed CO and facilitate C—C coupling [40,41]. Moreover, the presence of subsurface or interfacial suboxide species can promote CO_2 binding and activation in the initial steps of CO_2RR [42]. Overall, these observations indicate that the catalyst partially evolves into a metallic Cu structure during CO_2RR, with Cu^+ species likely formed at the surface or near-surface.

The additional peaks observed in the region of 30–35° 2θ do not correspond to any Cu catalyst phase but likely originate from residual electrolyte species that crystallized on the electrode surface after drying (e.g., hydrated KOH, K_2CO_3).

XPS spectra of Cu 2p region acquired for a selected sample (45 nm cube) after electrochemical test (Fig. S6a) show almost identical features to those of as-synthesized catalysts, confirming the presence of reduced Cu species (Cu^0 or Cu^+). Again, analysis of Cu LMM Auger region (Fig. S6b) pointed toward the presence of Cu^+ species rather than metallic Cu in the used catalyst.

We also acquired Raman spectra of GDEs prepared with nanocube catalysts before and after electrocatalytic tests in flow cell (Fig. S7). The

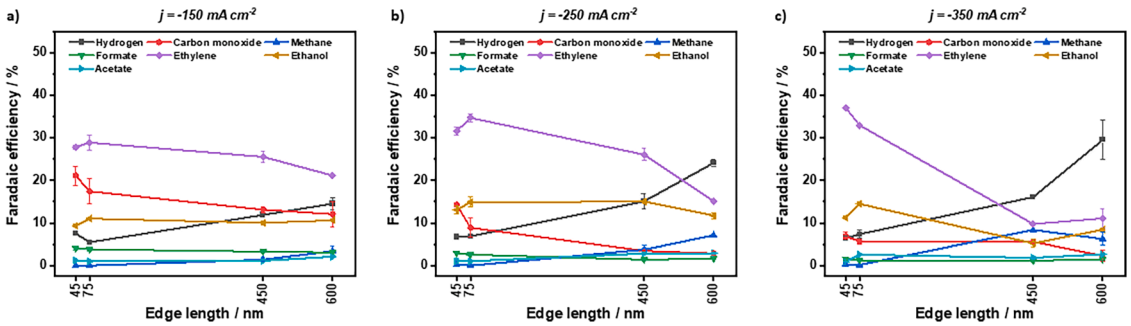

Fig. 3. Faradaic efficiencies of different Cu_2O nanocube electrocatalysts in flow cell obtained at different current densities: a) –150 mA cm^{-2}; b) –250 mA cm^{-2}; c) –350 mA cm^{-2}. Electrolyte: KOH 1 M.

spectra of fresh and used electrodes present similar features, in particular bands that can be ascribed to Cu-O vibration modes, indicating an oxidized surface of the catalysts, likely CuO [43,44].

The morphology of electrodes after the tests has been assessed by FESEM (Fig. 4).

Smaller cubes (45 nm and 75 nm, Fig. 4a, b) underwent the most severe changes in morphology during the electrochemical tests. While fresh samples exhibited well-defined cube nanostructure, after tests, most of the nanoparticles aggregated into clusters and interconnected particles. On the other hand, bigger cubes (450 nm and 600 nm, Fig. 4c, d) retained their shape under reaction conditions, despite a slight aggregation and reconstruction. These results are in accordance with the previous observation that aggregation and detachment of smaller cubes are accelerated by their higher mobility [18]. The higher selectivity toward CO_2RR in general, and C_2 products in particular, was previously attributed to the exposure of defects and residual oxygen species in the rearranged, fragmented catalyst [45,46].

3.4. Electrocatalytic tests in zero-gap cell

Although the flow cell setup allows screening the catalyst activity at industrially relevant current densities, zero-gap cells represent the most promising setup for CO_2 electrolysis in industrial applications [47,48]. Thus, we decided to verify the behavior of nanocubes in a zero-gap cell with an active area of 5 cm^2. We selected an industrially-relevant current density (j = –250 mA cm^{-2}) to first evaluate the FEs of nanocubes with different edge lengths. The results are reported in Fig. 5.

Compared to the results obtained in the flow cell reported in Fig. 3b, the FE_{H2} is substantially higher and less variable with cube edge length in the zero-gap cell. The FE_{CO} increases as the edge length increases up

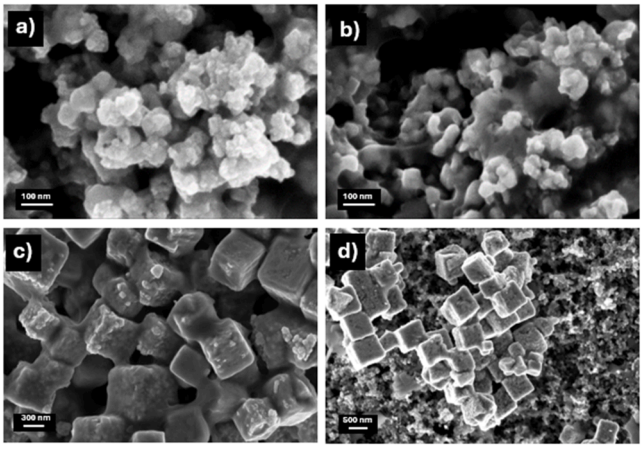

Fig. 4. FESEM of electrodes after electrocatalytic tests in flow cell (j = –250 mA cm^{-2}) prepared using Cu_2O nanocube electrocatalysts with different edge lengths: a) 45 nm; b) 75 nm; c) 450 nm; d) 600 nm.

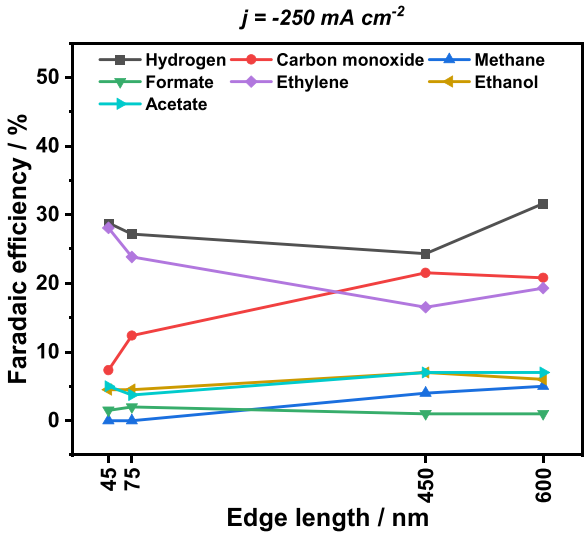

Fig. 5. Faradaic efficiencies of Cu_2O nanocube electrocatalysts in zero-gap electrolyzer at j = –250 mA cm^{-2}. Anolyte: $KHCO_3$ 0.1 M.

to the 450 nm cubes and then reaches a plateau; this trend is opposite to what we observed in the flow cell, further supporting that the catalyst selectivity is strongly dependent on the boundary testing conditions (electrolyte, cell type, etc.). On the other hand, FE_{C2H4} is highest (28 %) for the smallest cubes (45 nm), and then decreases for the 75 and 450 nm cubes. For the large cubes (450 and 600 nm), we observed the appearance of CH_4 with FEs ≈ 5 %, while this product was not detected for the small cubes. This finding is very similar to what we previously observed for the flow cell. Regarding the liquid products, formate was detected only in traces, while ethanol and acetate were found to be similar for all the samples, and the FE of each of these two products did not exceed 7 %.

Comparing these results with those obtained for the flow cell, we can observe a drastic reduction of FE for ethanol, whose FEs were ≈3 times higher in the flow cell, regardless of the cube size. Since the liquid products were collected in the anolyte, a fraction of ethanol could potentially be lost in the gas phase at the cathode side and therefore is not detected in our analysis.

The higher FE_{H2} and lower FE for C_2 products (ethylene, ethanol) obtained in the zero-gap cell as compared to the flow cell can be attributed to the highly alkaline electrolyte used in the flow-cell (KOH 1 M), which helps keep a high local pH. Local pH values above 10 promote the formation of C_{2+} products [49,50] by favoring *CO adsorption and HER suppression [51]. In contrast with flow cells, in zero-gap configurations, the local environment at the membrane surface strongly influences catalysis. As a result, the local pH depends on several variables, including the rate of OH^- generation and the ionic species transported

through the membrane. This, in turn, limits the ability to precisely control the local pH in this type of setup.

For industrial applications, not only activity and selectivity but also stability is an important factor to consider. Therefore, we selected the most selective catalyst for ethylene production, i.e., Cu_2O cube with an edge length of 45 nm, for a long-term test. For this purpose, we conducted the test with cesium bicarbonate instead of potassium bicarbonate as anolyte, since highly soluble Cs salts help delay salt precipitation and thus electrode deactivation [47,52,53]. The time evolution of gas products during the stability test is reported in Fig. 6.

In the first 4 h of the test, the FEs for the main products were constant: the main gas product was CO, with $FE_{CO} \approx 43$ %, while FE_{C2H4} was ≈ 14 %. The cell voltage was ≈ 3.6 V. In the remaining time of the test, we observed a strong decrease in the CO production with an increase of H_2 and C_2H_4 production until $t = 19$ h, where FE_{C2H4} dropped due to salt accumulation on the back of the electrode. The image of the GDE after test confirmed the deposition of salt in large parts of the electrode (Fig. S8a), supporting the hypothesis that salt deposition is responsible for electrode failure in MEA setups. On the other hand, the catalyst particles are present in form of aggregates with dimensions of tens of nm (Fig. S8b).

Although the use of $CsHCO_3$ as anolyte helps delay salt formation, FE_{CO} was significantly higher and FEC_{2H4} lower compared to the performance of the same catalyst (45 nm cubes) with $KHCO_3$ anolyte (reported in Fig. 5), pointing toward a critical role of the electrolyte in directing the selectivity among the different CO_2 reduction products. The effect arises from the ability of alkaline cations to modulate the local environment near the catalytic active site. In particular, electrolyte cations exhibit different buffering capacities near a negatively charged cathode surface: Cs^+ provides a lower local basicity than K^+ [54], which negatively affects ethylene formation in favor of carbon monoxide (see Fig. 5 and Fig. 6). For long-term operation, however, $CsHCO_3$ as the anolyte allows to reduce salt accumulation on the cathode, which would otherwise limit electrolyzer lifetime. Achieving FE_{C2H4} values comparable to those obtained in flow-cell systems will require further optimization of MEA design and operating conditions.

Strategies reported in the literature include the use of pure water as the anolyte while incorporating the necessary cations directly into the cathode catalyst layer [55,56], or operating with $KHCO_3$ anolyte while actively monitoring cation crossover. Before reaching the solubility limit of the cathode-side electrolyte, $KHCO_3$ can be replaced by pure water to reduce accumulated K^+ until it falls below the threshold at which catalytic performance is affected [57]. Achieving high FE_{C2_+} selectivity in zero-gap configurations therefore requires a careful balance between cation transport, local pH regulation, water availability, and salt management.

4. Conclusions

Cu_2O nanocubes with edge lengths ranging from 45 to 600 nm were successfully synthesized and evaluated as electrocatalysts for CO_2 reduction, with a focus on ethylene production. Screening in an alkaline flow cell setup at industrially relevant current densities (–150 to –350 mA cm^{-2}) revealed that smaller cubes (45 and 75 nm) achieved significantly higher Faradaic efficiencies (FEs) for C_2 products compared to larger cubes (450 and 600 nm). All samples underwent morphological reconstruction under high current densities. In a zero-gap electrolyzer, more representative of industrial systems, 45 nm cubes again exhibited the highest ethylene selectivity at $j = -250$ mA cm^{-2}. Durability tests using $CsHCO_3$ as the anolyte, aimed at mitigating salt precipitation, showed a trade-off: although catalyst stability improved, ethylene selectivity decreased compared to tests using $KHCO_3$ or the flow cell setup. These findings indicate that while smaller nanocubes are more selective for ethylene, their performance is highly dependent on the operating environment. Therefore, assessing catalyst behavior under industrially relevant conditions is essential for the development of scalable CO_2RR systems.

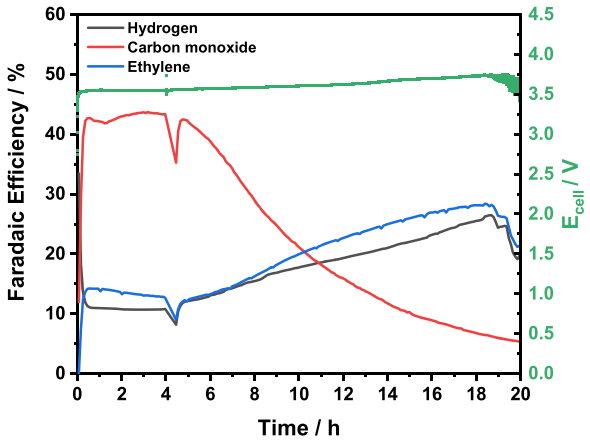

Fig. 6. Stability test of 45 nm Cu_2O nanocube electrocatalyst in zero-gap cell at $j = -250$ mA cm^{-2}. Anolyte: $CsHCO_3$ 0.1 M.

Declaration of generative AI and AI-assisted technologies in the manuscript preparation

During the preparation of this work the authors used ChatGPT (OpenAI) to check grammar and improve text readability. After using this tool, the authors reviewed and edited the content as needed and take full responsibility for the content of the published article.

CRediT authorship contribution statement

Marco Etzi: Writing – review & editing, Writing – original draft, Visualization, Validation, Supervision, Methodology, Investigation, Formal analysis, Data curation, Conceptualization. **Alessio Mezza:** Writing – review & editing, Visualization, Validation, Methodology, Investigation, Formal analysis, Data curation, Conceptualization. **Valentina Bugliarelli:** Writing – review & editing, Visualization, Validation, Methodology, Investigation, Formal analysis, Data curation. **Julien Dangbegnon:** Writing – review & editing, Validation, Methodology, Investigation, Formal analysis, Conceptualization. **Daniele Sassone:** Writing – review & editing, Methodology, Investigation. **Mattia Bartoli:** Writing – review & editing, Visualization, Methodology, Investigation, Formal analysis, Data curation. **Juqin Zeng:** Writing – review & editing, Methodology. **Angelica Chiodoni:** Writing – review & editing, Investigation. **Sergio Bocchini:** Supervision. **Adriano Sacco:** Supervision. **Candido Fabrizio Pirri:** Resources, Funding acquisition.

Declaration of competing interest

The authors have no conflicts of interest to declare.

Acknowledgements

This study was developed in the framework of the research activities carried out within the Project "Network 4 Energy Sustainable Transition—NEST", Spoke 4, Project code PE0000021, funded under the National Recovery and Resilience Plan (NRRP), Mission 4, Component 2, Investment 1.3— Call for tender No 1561 of 11/10/2022 of Ministero dell'Universita` e della Ricerca (MUR); funded by the European Union—NextGenerationEU. Juqin Zeng received the fund under the National Recovery and Resilience Plan (NRRP), Mission 4 "Education and Research" - Call for tender No 3264 of 28/12/2021 of Ministero dell'Universita` e della Ricerca (MUR) funded by the European Union—NextGenerationEU - Project code: IR0000027, CUP: B33C22000710006, Project title: iENTRANCE.

Supplementary materials

Supplementary material associated with this article can be found, in the online version, at doi:10.1016/j.electacta.2026.148114.

Data availability

Data will be made available on request.

References

[1] Y. Quan, J. Zhu, G. Zheng, Electrocatalytic reactions for converting CO2 to value-added products, Small. Sci. 1 (2021) 2100043, https://doi.org/10.1002/smsc.202100043.

[2] A. Bagger, W. Ju, A.S. Varela, P. Strasser, J. Rossmeisl, Electrochemical CO2 reduction: a classification problem, Chemphyschem 18 (2017) 3266–3273, https://doi.org/10.1002/cphc.201700736.

[3] S. Nitopi, E. Bertheussen, S.B. Scott, X. Liu, A.K. Engstfeld, S. Horch, B. Seger, I.E. L. Stephens, K. Chan, C. Hahn, J.K. Nørskov, T.F. Jaramillo, I. Chorkendorff, Progress and perspectives of electrochemical CO2 reduction on copper in aqueous electrolyte, Chem. Rev. 119 (2019) 7610–7672, https://doi.org/10.1021/acs.chemrev.8b00705.

[4] Y. Hori, R. Takahashi, Y. Yoshinami, A. Murata, Electrochemical reduction of CO at a copper electrode, J. Phys. Chem. B. 101 (1997) 7075–7081, https://doi.org/10.1021/jp970284i.

[5] R. Kortlever, J. Shen, K.J.P. Schouten, F. Calle-Vallejo, M.T.M. Koper, Catalysts and reaction pathways for the electrochemical reduction of carbon dioxide, J. Phys. Chem. Lett. 6 (2015) 4073–4082, https://doi.org/10.1021/acs.jpclett.5b01559.

[6] W. Tang, A.A. Peterson, A.S. Varela, Z.P. Jovanov, L. Bech, W.J. Durand, S. Dahl, J. K. Nørskov, I. Chorkendorff, The importance of surface morphology in controlling the selectivity of polycrystalline copper for CO2 electroreduction, Phys. Chem. Chem. Phys. 14 (2012) 76–81, https://doi.org/10.1039/c1cp22700a.

[7] A. Dutta, M. Rahaman, N.C. Luedi, M. Mohos, P. Broekmann, Morphology matters: tuning the product distribution of CO2 electroreduction on oxide-derived Cu foam catalysts, ACS. Catal. 6 (2016) 3804–3814, https://doi.org/10.1021/acscatal.6b00770.

[8] A.H.M. da Silva, S.J. Raaijman, C.S. Santana, J.M. Assaf, J.F. Gomes, M.T.M. Koper, Electrocatalytic CO2 reduction to C2+ products on Cu and CuxZny electrodes: effects of chemical composition and surface morphology, J. Electroanal. Chem. 880 (2021) 114750, https://doi.org/10.1016/j.jelechem.2020.114750.

[9] Y. Zhang, A. Özden, L. Gao, J.P. Hofmann, E.J.M. Hensen, The role of copper-oxide species in copper-catalyzed electrochemical CO2 reduction, ChemElectroChem. 12 (2025) e202500032, https://doi.org/10.1002/celc.202500032.

[10] Y. Hori, I. Takahashi, O. Koga, N. Hoshi, Selective formation of C2 compounds from electrochemical reduction of CO2 at a series of copper single crystal electrodes, J. Phys. Chem. B. 106 (2002) 15–17, https://doi.org/10.1021/jp013478d.

[11] G.L. De Gregorio, T. Burdyny, A. Loiudice, P. Iyengar, W.A. Smith, R. Buonsanti, Facet-dependent selectivity of Cu catalysts in electrochemical CO2 reduction at commercially viable current densities, ACS. Catal. 10 (2020) 4854–4862, https://doi.org/10.1021/acscatal.0c00297.

[12] K.J.P. Schouten, E. Pérez Gallent, M.T.M. Koper, Structure sensitivity of the electrochemical reduction of carbon monoxide on copper single crystals, ACS. Catal. 3 (2013) 1292–1295, https://doi.org/10.1021/cs4002404.

[13] F.S. Roberts, K.P. Kuhl, A. Nilsson, High selectivity for ethylene from carbon dioxide reduction over copper nanocube electrocatalysts, Angew. Chemie - Int. Ed. 54 (2015) 5179–5182, https://doi.org/10.1002/anie.201412214.

[14] K. Manthiram, B.J. Beberwyck, A.P. Alivisatos, Enhanced electrochemical methanation of carbon dioxide with a dispersible nanoscale copper catalyst, J. Am. Chem. Soc. 136 (2014) 13319–13325, https://doi.org/10.1021/ja5065284.

[15] R. Reske, H. Mistry, F. Behafarid, B. Roldan Cuenya, P. Strasser, Particle size effects in the catalytic electroreduction of CO2 on Cu nanoparticles, J. Am. Chem. Soc. 136 (2014) 6978–6986, https://doi.org/10.1021/ja500328k.

[16] A. Loiudice, P. Lobaccaro, E.A. Kamali, T. Thao, B.H. Huang, J.W. Ager, R. Buonsanti, Tailoring copper nanocrystals towards C2 products in electrochemical CO2 reduction, Angew. Chemie - Int. Ed. 55 (2016) 5789–5792, https://doi.org/10.1002/anie.201601582.

[17] P. Grosse, D. Gao, F. Scholten, I. Sinev, H. Mistry, B.Roldan Cuenya, Dynamic changes in the structure, chemical State and catalytic selectivity of Cu nanocubes during CO2 electroreduction: size and support effects, Angew. Chemie - Int. Ed. 57 (2018) 6192–6197, https://doi.org/10.1002/anie.201802083.

[18] P. Grosse, A. Yoon, C. Rettenmaier, A. Herzog, S.W. Chee, B.Roldan Cuenya, Dynamic transformation of cubic copper catalysts during CO2 electroreduction and its impact on catalytic selectivity, Nat. Commun. 12 (2021) 1–11, https://doi.org/10.1038/s41467-021-26743-5.

[19] K. Rossi, R. Buonsanti, Shaping copper nanocatalysts to steer selectivity in the electrochemical CO2 reduction reaction, Acc. Chem. Res. 55 (2022) 629–637, https://doi.org/10.1021/acs.accounts.1c00673.

[20] E. Mardones-herrera, C. Castro-castillo, K. Nanda, N. Veloso, F. Leyton, F. Martinez, N. Saez-Pizarro, D. Ruiz-Leon, M.J. Aguirre, F. Armijo, M. Isaacs, Reduced graphene oxide overlayer on copper nanocube electrodes steers the selectivity towards ethanol in electrochemical reduction of carbon dioxide, ChemElectroChem. (2022) 202200259, https://doi.org/10.1002/celc.202200259.

[21] T. Burdyny, W.A. Smith, CO2 reduction on gas-diffusion electrodes and why catalytic performance must be assessed at commercially-relevant conditions, Energy Environ. Sci. 12 (2019) 1442–1453, https://doi.org/10.1039/c8ee03134g.

[22] T.N. Nguyen, C.T. Dinh, Gas diffusion electrode design for electrochemical carbon dioxide reduction, Chem. Soc. Rev. 49 (2020) 7488–7504, https://doi.org/10.1039/d0cs00230e.

[23] E.W. Lees, B.A.W. Mowbray, F.G.L. Parlane, C.P. Berlinguette, Gas diffusion electrodes and membranes for CO2 reduction electrolysers, Nat. Rev. Mater. 7 (2022) 55–64, https://doi.org/10.1038/s41578-021-00356-2.

[24] M. Etzi, J. Dangbegnon, A. Chiodoni, C.F. Pirri, Impact of gas diffusion layer architecture on the performances of Cu-based electrodes for CO2 electroreduction to ethylene in flow reactors, J. CO2 Util. 83 (2024) 102772, https://doi.org/10.1016/j.jcou.2024.102772.

[25] L. Gatti, S. Verhovez, A. Mezza, M. Etzi, S. Stassi, C.F. Pirri, A. Sacco, Role of the binder in mitigating salt deposition in 100 cm 2 membrane electrode assembly CO 2 electrolyzers, Adv. Energy Sustain. Res. 202500312 (2025) 1–8, https://doi.org/10.1002/aesr.202500312.

[26] S. Popović, M. Smiljanić, P. Jovanovič, J. Vavra, R. Buonsanti, N. Hodnik, Stability and degradation mechanisms of copper-based catalysts for electrochemical CO2 reduction, Angew. Chemie - Int. Ed. 59 (2020) 14736–14746, https://doi.org/10.1002/anie.202000617.

[27] M. van der Veer, N. Daems, P. Cool, T. Breugelmans, From batch to flow: the effect of pH, current, and the crystal facets of Cu2O on electrochemical CO2 reduction, Sustain. Energy Fuels 8 (2024) 2504–2518, https://doi.org/10.1039/d4se00130c.

[28] I.C. Chang, P.C. Chen, M.C. Tsai, T.T. Chen, M.H. Yang, H.T. Chiu, C.Y. Lee, Large-scale synthesis of uniform Cu2O nanocubes with tunable sizes by in-situ nucleation, CrystEngComm. 15 (2013) 2363–2366, https://doi.org/10.1039/c3ce26932a.

[29] Y. Gao, L. Zhang, A.J.F. van Hoof, E.J.M. Hensen, On the surface-dependent oxidation of Cu2O during CO oxidation: Cu2+ is more active than Cu+, Appl. Catal. A Gen. 602 (2020) 117712 https://doi.org/10.1016/j.apcata.2020.117712.

[30] S. Quesada, L. Gatti, M. Alberghini, A. Tommasi, M. Etzi, A. Mezza, A. Sacco, F. C. Pirri, D. Sassone, A deeper understanding of flooding dynamics in gas diffusion electrodes for CO2 electrolyzer : how interfacial pressure shapes gas – liquid stability, Chem. Eng. J. 527 (2026) 171393, https://doi.org/10.1016/j.cej.2025.171393.

[31] N.S. Mcintyre, M.G. Cook, X-ray photoelectron studies on some oxides and hydroxides of cobalt, nickel, and copper, Anal. Chem. 47 (1975) 2208–2213, https://doi.org/10.1021/ac60363a034.

[32] M.C. Biesinger, B.P. Payne, A.P. Grosvenor, L.W.M. Lau, A.R. Gerson, R.S.C. Smart, Resolving surface chemical states in XPS analysis of first row transition metals, oxides and hydroxides: Cr, Mn, Fe, Co and Ni, Appl. Surf. Sci. 257 (2011) 2717–2730, https://doi.org/10.1016/j.apsusc.2010.10.051.

[33] M.C. Biesinger, Advanced analysis of copper X-ray photoelectron spectra, Surf. Interface Anal. 49 (2017) 1325–1334, https://doi.org/10.1002/sia.6239.

[34] E. Tosi Brandi, J. De Maron, A. Fasolini, N. Sangiorgi, A. Sangiorgi, M. Etzi, E. Scavetta, A. Sanson, F. Basile, Streamlining CO_2 photoelectrocatalytic conversion to C2+ products using CuMg-based LDH : a single-material photocathode strategy, Appl. Catal. B Environ. Energy. 385 (2026) 126276, https://doi.org/10.1016/j.apcatb.2025.126276.

[35] C.T. Dinh, T. Burdyny, G. Kibria, A. Seifitokaldani, C.M. Gabardo, F. Pelayo García De Arquer, A. Kiani, J.P. Edwards, P. De Luna, O.S. Bushuyev, C. Zou, R. Quintero-Bermudez, Y. Pang, D. Sinton, E.H. Sargent, CO2 electroreduction to ethylene via hydroxide-mediated copper catalysis at an abrupt interface, Science (80-.) 360 (2018) 783–787, https://doi.org/10.1126/science.aas9100.

[36] J.J. Velasco-Velez, J.J. Velasco-Velez, R.V. Mom, L.E. Sandoval-Diaz, L.J. Falling, C.H. Chuang, D. Gao, D. Gao, T.E. Jones, Q. Zhu, Q. Zhu, R. Arrigo, B. Roldan Cuenya, A. Knop-Gericke, A. Knop-Gericke, T. Lunkenbein, R. Schlögl, R. Schlögl, Revealing the active phase of copper during the electroreduction of CO2in aqueous electrolyte by correlating in situ X-ray spectroscopy and in situ electron microscopy, ACS Energy Lett. 5 (2020) 2106–2111, https://doi.org/10.1021/acsenergylett.0c00802.

[37] S.K. Matam, P.K. Sharma, E.H. Yu, C. Drivas, M.D. Khan, M. Wilding, N. Ramanan, D. Gianolio, M.A. Isaacs, S. Guan, P.R. Davies, C.R.A. Catlow, Operando X-ray absorption spectroscopic flow cell for electrochemical CO2 reduction: new insight into the role of copper species, Catal. Sci. Technol. (2024) 1070–1081, https://doi.org/10.1039/d4cy00602j.

[38] J.K. Dangbegnon, M. Etzi, J. Zeng, A. Chiodoni, C.F. Pirri, CO2 electroreduction towards ethylene on copper phosphate-derived catalysts in alkaline flow cell, Catal. Sci. Technol. 15 (2025) 2318–2326, https://doi.org/10.1039/d4cy01365d.

[39] Y. Lum, J.W. Ager, Stability of residual oxides in oxide-derived copper catalysts for electrochemical CO2 reduction investigated with 18O labeling, Angew. Chemie Int. Ed. 57 (2018) 551–554, https://doi.org/10.1002/ANIE.201710590.

[40] X. He, L. Lin, X. Li, M. Zhu, Q. Zhang, S. Xie, B. Mei, F. Sun, Z. Jiang, J. Cheng, Y. Wang, Roles of copper(I) in water-promoted CO2 electrolysis to multi-carbon compounds, Nat. Commun. 15 (2024), https://doi.org/10.1038/s41467-024-54282-2.

[41] Y.C. Chu, K.H. Chen, C.W. Tung, H.C. Chen, J. Wang, T.R. Kuo, C.S. Hsu, K.H. Lin, L.D. Tsai, H.M. Chen, Dynamic (Sub)surface-oxygen enables highly efficient carbonyl-coupling for electrochemical carbon dioxide reduction, Adv. Mater. 36 (2024) 2400640, https://doi.org/10.1002/ADMA.202400640.

[42] M. Favaro, H. Xiao, T. Cheng, W.A. Goddard, E.J. Crumlin, Subsurface oxide plays a critical role in CO2 activation by Cu(111) surfaces to form chemisorbed CO2, the first step in reduction of CO2, Proc. Natl. Acad. Sci. U. S. A. 114 (2017) 6706–6711, https://doi.org/10.1073/pnas.1701405114.

[43] M. Balkanski, M.A. Nusimovici, J. Reydellet, First order Raman spectrum of Cu2O, Solid. State Commun. 7 (1969) 815–818, https://doi.org/10.1016/0038-1098(69)90768-6.
[44] J. Chrzanowski, J. Irwin, Raman scattering from cupric oxide, Solid. State Commun. 70 (1989) 11–14, https://doi.org/10.1016/0038-1098(89)90457-2.
[45] H. Jung, S.Y. Lee, C.W. Lee, M.K. Cho, D.H. Won, C. Kim, H.S. Oh, B.K. Min, Y. J. Hwang, Electrochemical fragmentation of Cu 2 O nanoparticles enhancing selective C-C coupling from CO 2 reduction reaction, J. Am. Chem. Soc. 141 (2019) 4624–4633, https://doi.org/10.1021/jacs.8b11237.
[46] Q. Ren, N. Zhang, Z. Dong, L. Zhang, X. Chen, L. Luo, Structural evolution of Cu2O nanocube electrocatalysts for the CO2 reduction reaction, Nano Energy 106 (2023) 108080, https://doi.org/10.1016/j.nanoen.2022.108080.
[47] M. Sassenburg, M. Kelly, S. Subramanian, W.A. Smith, T. Burdyny, Zero-gap electrochemical CO2 reduction cells: challenges and operational strategies for prevention of salt precipitation, ACS. Energy Lett. 8 (2023) 321–331, https://doi.org/10.1021/acsenergylett.2c01885.
[48] A. Mezza, J. Zeng, M. Etzi, D. Sassone, F.C. Pirri, A. Sacco, Evaluating bicarbonate electrolyzer configurations for energy-efficient formate production, Adv. Sustain. Syst. 2500098 (2025) 1–8, https://doi.org/10.1002/adsu.202500098.
[49] D. Raciti, M. Mao, J.H. Park, C. Wang, Local pH effect in the CO2 reduction reaction on high-surface-area copper electrocatalysts, J. Electrochem. Soc. 165 (2018) F799, https://doi.org/10.1149/2.0521810jes.
[50] T. Wu, H. Bu, S. Tao, M. Ma, Determination of local pH in CO2 electroreduction, Nanoscale 16 (2024) 3926–3935, https://doi.org/10.1039/d3nr06357g.
[51] K. Xiang, F. Shen, Y. Fu, L. Wu, Z. Wang, H. Yi, X. Liu, P. Wang, M. Liu, Z. Lin, H. Liu, Boosting CO2 electroreduction towards C2+ products via CO* intermediate manipulation on copper-based catalysts, Environ. Sci. Nano. 9 (2022) 911–953, https://doi.org/10.1039/d1en00977j.
[52] S. Garg, Q. Xu, A.B. Moss, M. Mirolo, W. Deng, I. Chorkendorff, J. Drnec, B. Seger, How alkali cations affect salt precipitation and CO2 electrolysis performance in membrane electrode assembly electrolyzers, Energy Environ. Sci. 16 (2023) 1631–1643, https://doi.org/10.1039/d2ee03725d.
[53] J. Biemolt, J. Singh, G.P. Vergel, H.M. Pelzer, T. Burdyny, Preventing salt formation in zero-gap CO 2 electrolyzers by quantifying cation accumulation, ACS. Energy Lett. 10 (2025) 807–814, https://doi.org/10.1021/acsenergylett.4c03242.
[54] F. Zhang, A.C. Co, Direct evidence of local pH change and the role of Alkali cation during CO2 electroreduction in aqueous Media, Angew. Chemie - Int. Ed. 59 (2020) 1674–1681, https://doi.org/10.1002/anie.201912637.
[55] B. Endrődi, A. Samu, E. Kecsenovity, T. Halmágyi, D. Sebők, C. Janáky, Operando cathode activation with alkali metal cations for high current density operation of water-fed zero-gap carbon dioxide electrolysers, Nat. Energy. 6 (2021) 439–448, https://doi.org/10.1038/s41560-021-00813-w.
[56] J. Fan, B. Pan, J. Wu, C. Shao, Z. Wen, Y. Yan, Y. Wang, Y. Li, J. Fan, B.B. Pan, C. C. Shao, Z.Y. Wen, Y.C. Yan, Y.H. Wang, Y.G. Li, J.L. Wu, Immobilized tetraalkylammonium cations enable metal-free CO2 electroreduction in acid and pure water, Angew. Chemie Int. Ed. 63 (2024) e202317828, https://doi.org/10.1002/ANIE.202317828.
[57] P. Gyenes, A.A. Samu, D. Hursán, V. Józo, A. Serfozo, B. Endrodi, C. Janáky, Flooding revisited: electrolyte management ensures robust electrochemical CO2 reduction, Energy Environ. Sci. 18 (2025) 7124, https://doi.org/10.1039/d5ee01464f.